Joule

Article

TEMPO bulk passivation boosts the performance and operational stability of rapid-annealed FAPI perovskite solar cells

Graphical abstract

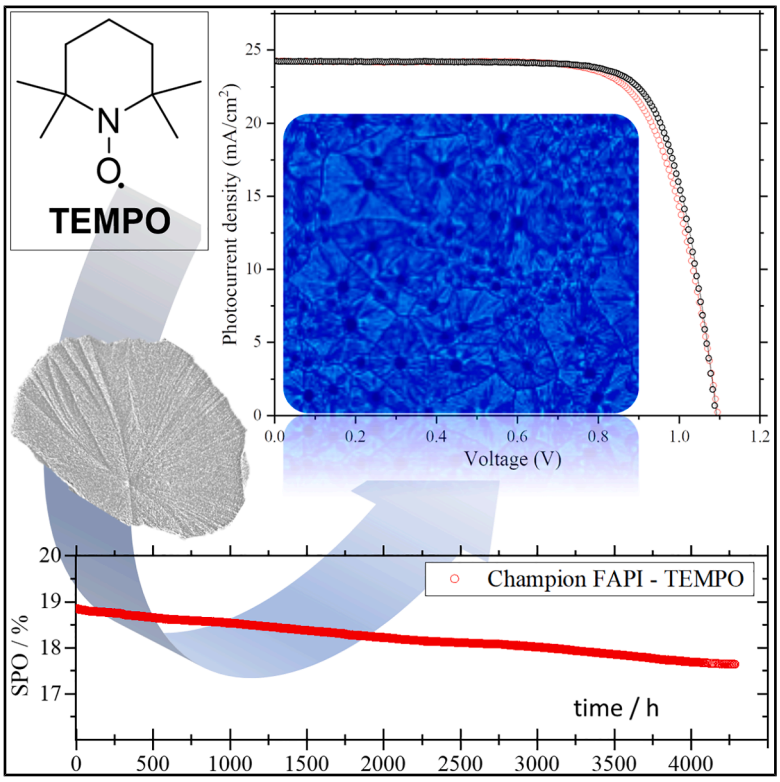

Authors

Sandy Sánchez-Alonso, Lukas Pfeifer, Ornella Vaccarelli, ..., Rafael Ferragut, Kevin Sivula, Michael Graetzel

Correspondence

sandy.sanchezalonso@epfl.ch

In brief

Perovskite solar cells could make ultra-cheap, flexible solar panels, but they quickly degrade in sunlight and heat. Adding a trace of the TEMPO molecule and zapping the film with a half-second infrared flash mends hidden microscopic seams, pushing efficiency past 20% and keeping it there for months. Because the step is quick, solvent-less, and roll-to-roll ready, it points the way from lab discovery to durable, lightweight solar sheets made at industrial scale.

Highlights

- TEMPO additive lifts FAPI perovskite PCE above 20% via 0.6 s flash-IR annealing
- Devices retain >90% of their initial efficiency after 4,296 h light and heat stress
- Bulk defect density stays low; TEMPO mainly heals grain-boundary recombination sites
- Process is antisolvent-free, roll-to-roll compatible for lightweight solar modules

Sánchez-Alonso et al., 2025, Joule 9, 101972
July 16, 2025
https://doi.org/10.1016/j.joule.2025.101972

CellPress

Joule

CellPress
OPEN ACCESS

Article

TEMPO bulk passivation boosts the performance and operational stability of rapid-annealed FAPI perovskite solar cells

Sandy Sánchez-Alonso,[1,2,5,*] Lukas Pfeifer,[1] Ornella Vaccarelli,[3] Christophe Gisler,[3] Jean Hennebert,[3] Felix T. Eickemeyer,[1] Rafael Ferragut,[4] Kevin Sivula,[2] and Michael Graetzel[1]

[1]Laboratory of Photonics and Interfaces, Institute of Chemistry and Chemical Engineering, École Polytechnique Fédérale de Lausanne, 1015 Lausanne, Switzerland

[2]Laboratory for Molecular Engineering of Optoelectronic Nanomaterials, Institute of Chemistry and Chemical Engineering, École Polytechnique Fédérale de Lausanne, 1015 Lausanne, Switzerland

[3]Institute of Artificial Intelligence and Complex Systems, School of Engineering and Architecture of Fribourg, University of Applied Sciences and Arts of Western Switzerland, 1700 Fribourg, Switzerland

[4]L-NESS and Department of Physics, Politecnico di Milano, 22100 Como, Italy

[5]Lead contact

*Correspondence: sandy.sanchezalonso@epfl.ch

https://doi.org/10.1016/j.joule.2025.101972

CONTEXT & SCALE Perovskite solar cells could slash solar costs, yet their fragile films limit real-world use. Our study adds a trace of the benign radical TEMPO and cures the film with a 0.6 s flash-infrared pulse, giving phase-pure FAPI devices that top 20% efficiency and >90% of it being retained after 4,200 h in continuous operando conditions. The result shows that grain-boundary defects—not the perovskite lattice—drive long-term decay and that they can be tamed in a high-speed, antisolvent-free process.

Because the chemistry is simple and low energy, and the curing step aligns with roll-to-roll coating, this route could cut the carbon payback of solar modules to months and enable lightweight, flexible panels for buildings and mobility. Key challenges are replacing or safely encapsulating lead, scaling the method to meter-wide uniformity, and certifying outdoor durability, but the path to commercial pilot lines is now defined with this work.

SUMMARY

In this work, we present a high-performance, stable formamidinium lead iodide (FAPI) perovskite solar cell (PSC) achieved through the use of 2,2,6,6-tetramethylpiperidinyloxyl (TEMPO) bulk passivation and rapid photonic annealing. Utilizing flash infrared annealing (FIRA), we fabricated TEMPO-FAPI PSCs with a power conversion efficiency (PCE) exceeding 20%, exceeding the prior state of the art for this process. The TEMPO additive promotes enhanced crystallization dynamics, yielding films with improved homogeneity and reduced defect densities, as confirmed by photoluminescence (PL), profilometry, and positron annihilation lifetime spectroscopy (PALS). Stability testing under ISOS protocols demonstrated that the TEMPO-FAPI devices retained over 90% of their initial PCE after 4,296 h of operational and thermal stress, showing unprecedented longevity for a rapid processing technique. TEMPO's primary effect on passivating grain boundaries and surface defects is evidenced by a significantly reduced non-radiative recombination rate and low defect density, establishing this molecule as a promising additive for scalable, durable FAPI PSC manufacturing.

INTRODUCTION

Metal halide perovskites have rapidly emerged as promising candidates for next-generation thin-film solar cells due to their remarkable power conversion efficiencies (PCEs), surpassing many traditional photovoltaic (PV) technologies.[1–4] Recent advancements in the stability of perovskite devices have further fueled their potential for large-scale and sustainable energy applications.[5,6] Nevertheless, significant challenges remain to match the long-term stability of established PV technologies, such as silicon-based solar cells.[7] Achieving commercial viability for perovskite cells requires innovative solutions in both processing methods and compositional engineering to stabilize the material's active phases.[8]

Among perovskite compositions, the black phase of formamidinium lead iodide (referred as FAPI) has demonstrated notable potential due to its high PCE and improved thermal stability.[9–11] However, FAPI's desirable perovskite phase is prone to phase instability at room temperature, often converting to non-photoactive forms that degrade performance.[12–15] Previous studies have shown that compositional modifications, such as incorporating formate ions or blending with other halides, can effectively stabilize this black phase by reducing defects that promote phase transitions.[16–18] Yet, achieving stability requires highly controlled processing techniques that not only improve film quality but also preserve phase stability under operating conditions.[19,20]

A recurring approach to stabilizing FAPI involves cation alloying, which optimizes its structural order and reinforces phase stability.[21,22] This phenomenon is influenced by orbital ordering, wherein specific *d* orbitals on the cation site become preferentially occupied, indirectly affecting phase stability through structural modifications such as Jahn-Teller distortions.[23,24] These distortions—driven by factors like cation-anion interactions, local cation arrangement, and octahedral tilting—exert chemical pressure on the lattice, promoting stable phases.[25] However, such structural adjustments during crystal growth can introduce vacancies and defects, which act as recombination centers that hinder device performance by promoting ion migration.[26] Thus, minimizing defect density during crystallization is critical for achieving both structural and operational stability in perovskite solar cells.[21,27–30]

In this context, rapid annealing methods are particularly attractive for large-scale manufacturing due to their compatibility with high-throughput processes.<u>[24,31–33]</u> Flash infrared annealing (FIRA) has emerged as a powerful tool for perovskite film processing, allowing for controlled crystallization on subsecond timescales, which is advantageous for minimizing thermal degradation and ensuring uniform film quality.[34–39] In previous work, we demonstrated that FIRA could stabilize the black phase of FAPI within 640 ms of annealing, achieving impressive PCE values and enhanced operational stability. However, further advancements in passivation are necessary to address intrinsic defects that compromise long-term device stability.[19]

To address this, we explored the use of 2,2,6,6-tetramethylpiperidinyloxyl (TEMPO) as a bulk passivator in FAPI perovskites films processed using the FIRA method. Additionally, devices with an NIP architecture were fabricated and analyzed. TEMPO, unlike traditional ammonium-based passivators, interacts with both Pb^{2+} and FA^{+} ions in solution, facilitating a more uniform nucleation process and enhancing crystallinity across the film.[40] Bulk passivation with TEMPO has shown promise in optimizing crystallization dynamics, reducing interfacial defects, and increasing film compactness, which are essential for improving device stability and performance.[33,41]

Consequently, this study investigates TEMPO's effect on crystallization, defect mitigation, and operational stability, employing advanced characterization techniques, such as positron annihilation lifetime spectroscopy (PALS), which is used for analyzing atomic-level defects and has demonstrated success in applications involving semiconductors and metals.[42–45] In PALS studies, positrons are implanted into the material under investigation and lose energy through inelastic interactions until reaching thermal equilibrium, at which point they exhibit quantum behavior and can interact with the crystal. In defect-free crystals, the positron wave function forms a delocalized Bloch state, whereas in the presence of defects, such as vacancies, it becomes localized. PALS measures the time between positron implantation—synchronized with the buncher pulse—and annihilation, detected by a scintillator when one of the two 511 keV gamma rays (m_0c^2) is emitted. Reduced electron density at vacancy sites increases positron lifetime compared to defect-free crystals.

The lattice defect studies are complemented by optical observations of the FIRA-processed microstructured films and the high-throughput data acquisition setup (see methods). In synergy with the ease of optical film characterization, this work introduces Shannon entropy as a novel metric for analyzing morphological uniformity.[19,46] Shannon entropy, originally rooted in information theory and signal processing, measures randomness or unpredictability within a dataset.[47–49] Using this method, a total of 3,000 optical microscopy images were analyzed to calculate the entropy values, providing a robust dataset for quantifying the film morphology homogeneity, which directly impacts device performance. Therefore, our findings offer insights into the relationships between processing conditions, crystallization mechanisms, and material properties, with TEMPO showing notable effectiveness in enhancing PCE, exceeding the prior state of the art for the FIRA process and stabilizing FAPI films processed by FIRA.[50–52] By integrating additive-based passivation with rapid annealing, we provide a scalable approach to manufacturing durable, high-performance perovskite solar cells, marking a significant step forward in the commercial viability of perovskite-based photovoltaics.

RESULTS AND DISCUSSION

Contrary to conventional ammonium-based passivation materials such as octylammonium iodide, which primarily target surface defects, TEMPO offers a broader functional scope. TEMPO and its derivatives create a mild oxidizing environment and interact with both Pb^{2+} and FA^{+} ions.[53] This interaction facilitates defect passivation without significantly altering the chemical state while simultaneously promoting uniform nucleation by forming transient complexes that act as nucleation centers.[54,55] In this study, we added TEMPO at 1 wt % to the precursor solution to examine its influence on film morphology, defect mitigation, and device performance. We selected a FAPI perovskite composition without inorganic cations as a more sustainable choice.[56]

Here, we extended the Shannon entropy concept to quantify the degree of order in the crystallization patterns of perovskite films (Methods S1). As shown in Figure 1A, the addition of TEMPO to $FAPbI_3$ (FAPI) perovskite films resulted in a measurable decrease in Shannon entropy values, indicative of enhanced morphological uniformity during the crystallization process. Figure 1B illustrates representative mean values of optical images (top row) alongside corresponding heatmaps (middle row) and local entropy deviation maps (bottom row) for both film conditions. The heatmaps highlight the contrast in defect spots of the grain domains, revealing

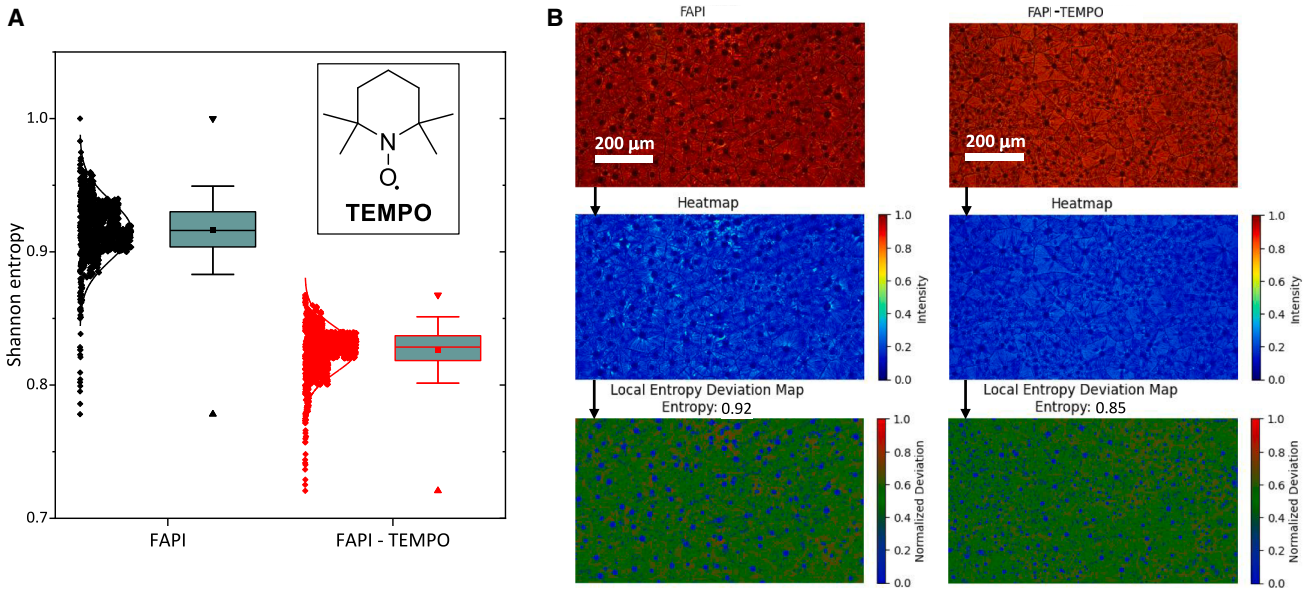

Figure 1. Shannon entropy-based analysis of film morphology for FAPI and FAPI–TEMPO

(A) Shannon entropy analysis of film morphology, with an inset of the chemical structure of TEMPO.

(B) Comparison of film morphology and entropy mapping for FAPI (left) and FAPI-TEMPO (right). The top row presents optical images of the films, followed by heatmaps (middle row) and local entropy deviation maps (bottom row). Scale bar: 200 µm.

disruptions in radial preferential growth. Along with the entropy deviation maps, they confirm a lower local entropy (0.85) in the TEMPO-treated FAPI film compared to the pristine FAPI film (0.92), emphasizing a more uniform grain arrangement upon TEMPO incorporation. Notably, the pristine film exhibits greater pixel-level deviations in Shannon entropy, suggesting a more defective microstructure as further supported by extended image processing and analyses for six selected images in Figure S1. Despite these differences, both samples maintain compact spherulite-like morphologies, a characteristic of photonic (FIRA) annealing.[39] Their comparable grain domain shapes make image-analysis techniques particularly effective for quantitative assessment.[22,39]

We then manufactured devices using standard NIP configuration, using FIRA for the perovskite wet film crystallization, as mentioned in the introduction. In this device architecture, the incorporation of a mesoporous layer enhances charge extraction and provides beneficial interfacial properties.[57] This is particularly relevant under rapid annealing conditions, where poor surface wettability can be a limiting factor.[58] The results of the manufactured devices are shown in Figure 2A, with a statistical distribution of the PV parameters collected from 30 PSCs of the reference (FAPI) and target (FAPI-TEMPO) group. We used phenethylammonium iodide (PEAI) passivation as our standard for the perovskite/HTM interface.[59,60] PEAI was selected as the standard passivation agent for the perovskite/HTM interface based on an optimization study, which showed superior device performance compared to pristine FAPI and other commonly used passivators such as OAI (octyl ammonium iodide) and FAI (formamidine iodide) (see Figure S2). Overall, the devices fabricated with FAPI-TEMPO demonstrated superior performance, achieving the highest efficiency reported so far using antisolvent (AS)-free methods with a film processing time under 640 ms.[34,61,62] As expected, the devices manufactured with pure FAPI perform poorly compared to FAPI-TEMPO.

Notably, the *V*oc values increase from an average of 1020–1070 V and the FF (%) from 69 to 73, resulting in an average PCE of 17% and 19% for FAPI and FAPI-TEMPO, respectively. A minor difference of 0.1 mA in Jsc occurs showing only a small improvement for the FAPI-TEMPO approach. The *JV* curve of the obtained champion cell revealed a PCE of 20.16% (Figure 2B), with further room for enhancement, particularly in terms of FF. The cross-sectional scanning electron microscopy (SEM) image of a device fabricated with a FAPI-TEMPO film (Figure 2C) shows a homogeneous and monolithic perovskite film with a thickness of ~700 nm. The incident photon-to-current efficiency (IPCE) in Figure 2D exhibits a similar *J*sc to that observed in the *JV* curve of the champion cell, with quite balanced photoconversion for all absorbed wavelengths and in agreement with the optical band gap reported for FAPI material.[63]

To validate the long-term operational stability of the devices, we employed adapted ISOS L-1, L-2, and L-3 protocols (see methods).[64] First, steady-state power output (SPO) measurements were recorded under maximum-power point tracking (MPPT) tracking at 1 sun, 35°C, in an inert atmosphere. Figure 3A shows that the champion device experienced only 6% degradation after 4,292 h. This is the best stability reported to date for pure FAPI MACl-free perovskite-based PSCs not using an AS process. Figure S3 shows *JV* curves after extended stress, illustrating minimal degradation. For further confirmation, Figure 3B displays normalized PCE values for six control and target devices, showing an average SPO loss of 17% after 2,500 h for FAPI devices and only 10% for FAPI - TEMPO devices after 4,292 h. The absolute SPO values are shown in Figure S4.

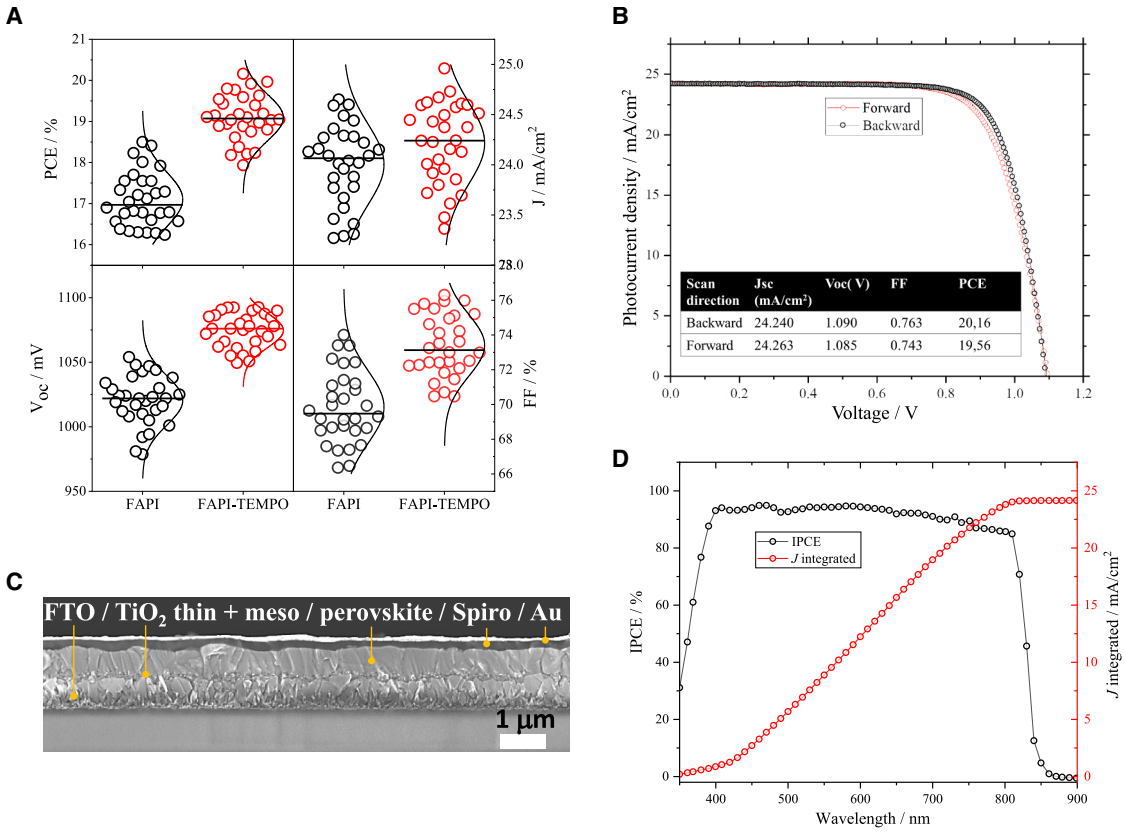

Figure 2. Performance statistics and champion-device characterization of FAPI and FAPI-TEMPO PSCs

(A) Statistical analysis of the *JV* parameters of FAPI and FAPI-TEMPO devices.

(B) *JV* curves of the champion target device (FAPI-TEMPO).

(C) Cross-sectional SEM image of a manufactured target PSC.

(D) IPCE and integrated J_{sc} curves of the champion target device.

Using an adapted ISOS L-3 protocol, Figure 3C shows the devices subjected to an 85°C MPPT scan in an inert atmosphere, with average losses of 27% for FAPI and 8% for FAPI-TEMPO over 250 h. Specifically, for the modified ISOS-L3 protocol, continuous illumination at 85°C with MPPT and an inert atmosphere (RH < 0.1%) were used. An additional stress test under 35% RH and 35°C with unencapsulated devices resulted in higher degradation than at 85°C and 0% RH, as shown in Figure S5. However, *in situ* optical images (Figure 3D) reveal only minor point defects in FAPI films under these conditions, as highlighted in the zoomed-in view at 35% RH exposure. For a more detailed observation, Figure S6 presents higher-resolution images of Figure 3D. While the morphological changes may not be visually striking at the resolution shown in Figure 3D, they are still significant enough to impact device performance due to phase instability. This is evidenced by the presence of a low-intensity Bragg δ-phase reflection ($2\theta = 11.8°$) in the XRD patterns of the stressed FAPI films presented in Figure S7.

After conducting extensive tests to assess the long-term stability of our devices, we focused on analyzing the difference TEMPO makes to the perovskite films to rationalize the improved performance of the target devices. We used a large amount of data points to ensure the robustness of our analyses as we examined the photophysical and morphological film features. Figure 4A presents the time-resolved photoluminescence (TRPL) measurements of 16 FAPI and FAPI-TEMPO films, while Figure 4B illustrates the estimated lifetime distribution. Through biexponential fitting, we determined a charge lifetime before recombination of approximately 700 ns (±88.7) for FAPI-TEMPO and 237 ns (±47.1) for FAPI, highlighting a significant difference. Consistently, the photoluminescence quantum yield (PLQY) measurements, depicted in Figure 4C for 40 films of each condition, corroborate the TRPL results, indicating an average increase of 2.5% going from FAPI to FAPI-TEMPO. Further PLQY analyses and results can be found in the supplemental information and in Tables S1 and S2. In Figure 4D, we represent the average surface roughness (*Ra*) for 10 films of each condition, measured in an area of 2 mm^2. The *Ra* of FAPI-TEMPO is around 56 nm and FAPI 78 nm, denoting a significant topology contrast that can directly cause the lower FF and *Voc* for pure FAPI in the fabricated devices (Figure 1). More details of the profilometric 2D maps for all samples can be seen in Figure S8.

Film crystallization in FIRA is driven by infrared (IR) irradiation, inducing structural transformations through kinetic changes.[35] During crystal growth, mass transport at the growing solid-liquid

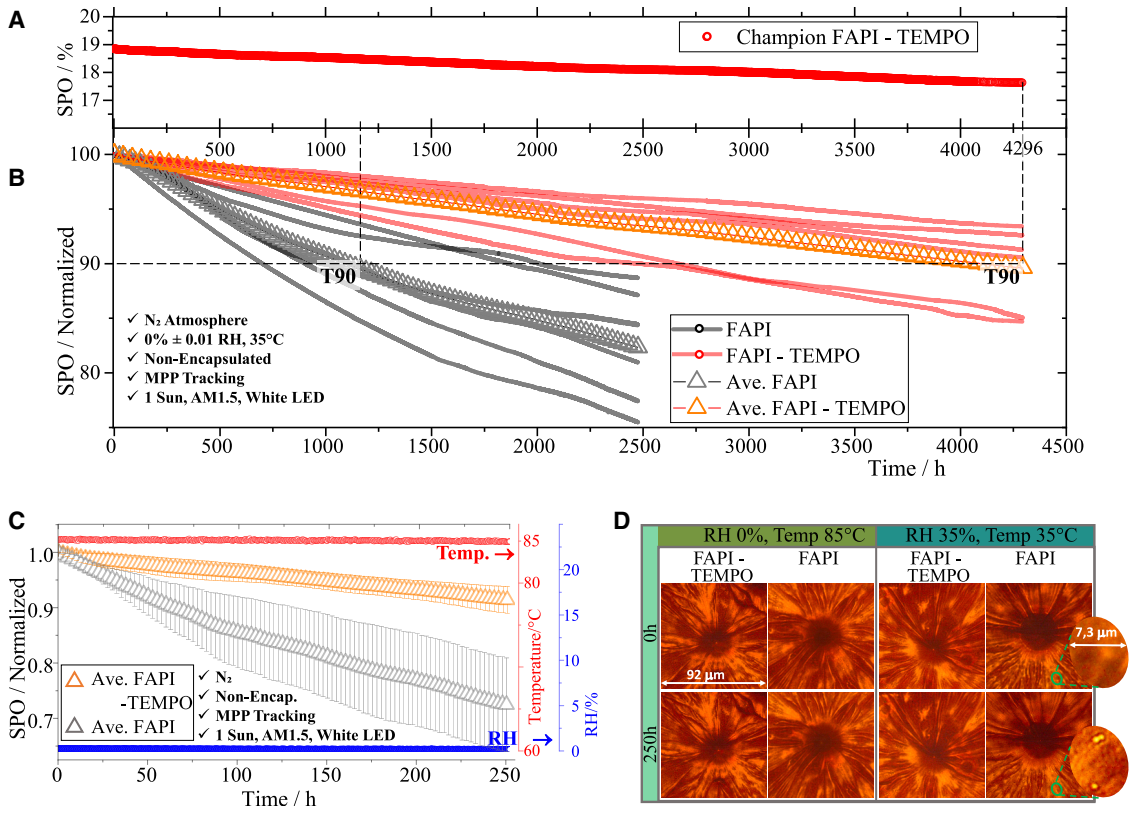

Figure 3. Enhanced operational and environmental stability of FAPI-TEMPO devices and films compared with pristine FAPI

(A) SPO over 4,296 h of a target device (1 sun) showing minimal degradation over time.

(B) Normalized SPO comparison between FAPI and FAPI-TEMPO devices, indicating enhanced stability for TEMPO-treated cells, with T90 (90% of initial PCE) exceeding 4,296 h.

(C) SPO accelerated aging conditions (85°C, 0% RH), with FAPI-TEMPO showing substantially improved stability compared to untreated FAPI.

(D) Optical images of FAPI and FAPI-TEMPO films under varying temperature and humidity conditions (0% RH at 85°C, 35% RH at 35°C, non-encapsulated), highlighting reduced degradation and fewer defects in the TEMPO-treated films after exposure for 250 h. All tests were conducted under 1 sun AM1.5 illumination using an LED array as the light source. The humidity test was performed by introducing moist air into the atmosphere (see methods).

interface shifts from front to secondary nucleation, producing dense branching structures.[33] It promotes the formation of spherulite domains with radial growth, as shown in the SEM images in Figure 4E, where FAPI samples reveal internal grain inhomogeneities. The red circle in the left SEM image highlights deviations from the ideal radial growth pattern within the domains. Spherulite microstructure variations can be analyzed through envelope growth (2D spherical) and internal anisotropy while having a similar crystal structure as characterized by GIWAXS analysis (Figure S9). The GIWAXS 2d plot shows that TEMPO-treated samples exhibiting a slightly enhanced crystallinity and preferred orientation, as evidenced by the sharper diffraction peaks in the integrated profiles.

Theoretical models often assume isotropic grain boundaries, yet real boundaries exhibit anisotropy, significantly influencing crystallization growth dynamics and mass transport.[35,65] Achieving a balanced composition for compact branching and linear growth is essential and can be effectively assessed through optical image processing techniques. Shannon entropy and computable information density (CID) analyses (methods; Methods S1: pixel detection algorithms method) show untreated FAPI films have higher CID values compared to TEMPO-treated ones, indicating greater internal inhomogeneity (Figure S10). Shape analyses (Figure S11; Methods S1) reveal no significant differences in domain shapes, confirming that the observed structural differences stem from internal grain-domain inhomogeneities.

TEMPO plays a crucial role in modulating the crystallization process by altering the growth envelope, directly impacting the homogeneity of the solution-phase crystallization dynamics. TEMPO interacts with Pb^{2+} and FA^{+} ions, influencing nucleation kinetics and crystal growth pathways.[53] As a result, TEMPO modifies the preferential growth directions and stabilizes the crystallization front, mitigating abrupt variations in grain formation and reducing anisotropic growth tendencies. ToF-SIMS analysis (Figure S12) localizes a TEMPO derivative, TEMPOH (2,2,6,6-tetramethylpiperidine-1-oxyl hydroxide), at the bottom interface of the film, further supporting its involvement in nucleation control. The presence of this species was confirmed by mass spectrometry (Figure S13) and electron paramagnetic resonance analysis (Figure S14). The interaction of TEMPO(H) with the growing perovskite grains reduces the formation of

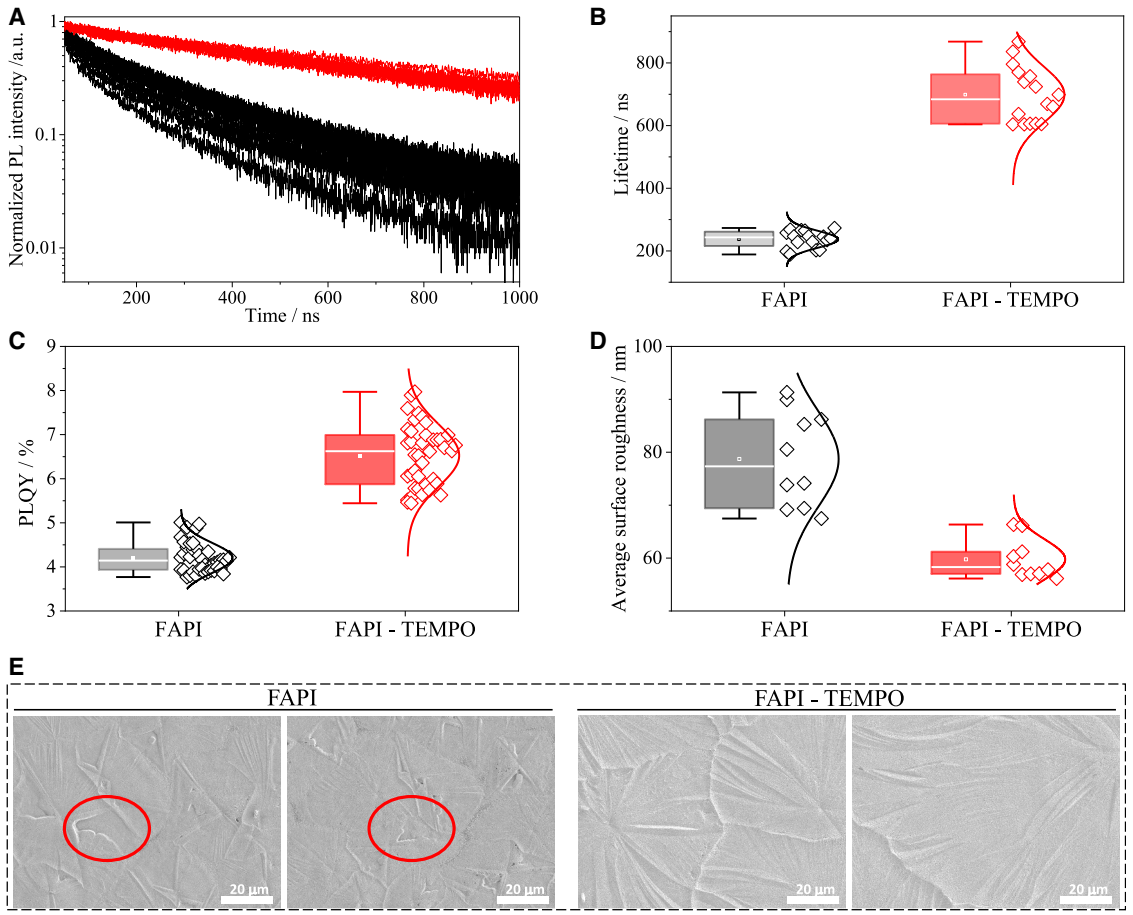

Figure 4. Time-resolved photoluminescence (TRPL), lifetime distribution, PLQY, surface roughness, and SEM images of FAPI and FAPI-TEMPO films

(A) TRPL measurements of 16 FAPI (black) and 16 FAPI-TEMPO films (red).

(B) Lifetime distribution calculated from (A).

(C) PLQY data of FAPI and FAPI-TEMPO films.

(D and E) (D) Average surface roughness (R_a) and (E) SEM top-view images of FAPI and FAPI-TEMPO films. (Red ovals in the two SEM images on the left highlight grain inhomogeneities of the FAPI samples).

pinholes and leads to a more uniform, defect-minimized film, ultimately enhancing performance and stability. TEMPO mitigates phase instability by promoting the formation of more uniform and compact films. Since defects at grain domain interfaces are energetically more susceptible to phase degradation, the improved film morphology induced by TEMPO helps to reduce these degradation pathways.

To further integrate additive-based passivation strategies with advanced defect characterization to bridge the gap between molecular engineering FAPI-TEMPO films, we employed PALS. Positrons implanted in these samples first thermalize without annihilation, then diffuse distances on the order of 50–100 nm inside the crystallites, which is the extension radius of the positron wave function, giving a refined characterization of the crystal defects such as vacancies (see methods and Methods S2). As for the studied films, which feature spherulite grain domains averaging 200 μm in diameter and are internally composed of smaller, oriented crystallites ranging from 1 to 5 μm,[40] the probability of a positron reaching the grain boundary is extremely low.

Figures 5A and S15 display the measured positron lifetime spectra for the FAPI-TEMPO and FAPI samples, respectively. Both measurements were conducted at a positron implantation energy of 8 keV. The spectra exhibit remarkably similar shapes for both samples. Mathematically, these spectra are represented by the function $S(t)$, given in Equation 1, and are affected by the convolution of the instrumental resolution function, $R(t)$,[66] with a sum of n exponential decay components, along with a low constant background B.

$$S(t) = \left[\sum_{i=1}^{n} \frac{I_i}{\tau_i} e^{-t/\tau_i}\right] * R(t) + B \qquad \text{(Equation 1)}$$

where I_i and τ_i represent the intensity and lifetime values of a given component, respectively. The resolution function, $R(t)$, is

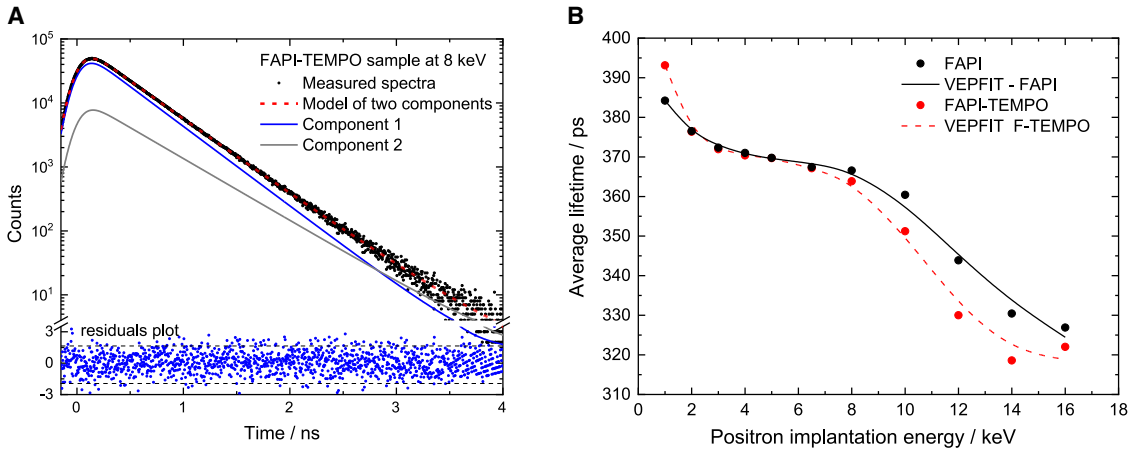

Figure 5. Positron lifetime spectrum and implantation-energy dependence of average lifetime for FAPI and FAPI-TEMPO samples

(A) Positron lifetime spectrum of a FAPI-TEMPO sample measured with 8 keV positron implantation energy.

(B) Average positron lifetime as a function of the positron implantation energy in FAPI and FAPI-TEMPO samples. Our analysis averages spectral data exceeding 10^7 counts for both samples, ensuring robust results.

modeled as the sum of two Gaussian functions, as explained in the methods section. To extract information from the measured data, the PALSfit software was used for deconvolution and fitting.[67] The FAPI samples are best fitted using two lifetime components (n = 2). The analysis of the positron lifetime spectra suggests vacancies as the primary defect type. The fitting parameters—intensities and lifetimes—are listed in Table 1. The results are robust, supported by an optimal statistical count of 10^7 events per spectrum.

Figure 5B presents the depth profile of the average positron lifetime at different implantation energies obtained from these samples, which is the weighted average defect size across sample thickness (see Methods S2). Figure S16 also shows that in the FAPI sample, the ideal region for analysis is between 6.5 and 8 keV, where about 97% of the positrons are implanted and thermalized within the films studied.

The analysis of the results is compatible with the hypothesis of the one defect standard trapping model (STM),[66,68] predicting a positron trapping rate, proportional to the vacancy concentration n:

$$n = K_D/\mu_V \qquad \text{(Equation 2)}$$

where μ_V is the defect-specific trapping coefficient (typically assumed to be 2×10^{15} s^{-1} in semiconductors, perovskites, and oxides[69]) and κ_D is the positron trapping rate. The defect density N presented in Table 1 was, therefore, calculated by multiplying the defect concentration n by the density of atoms in the MAPI perovskite structure ($\approx2\times10^{22}$ atoms/cm^3).

Assuming one defect type, the STM (see Methods S2) indicates two annihilation channels: the bulk and the defect. The defect lifetime component τ_2 at ~444 ps is observed (Table 1)—attributed to vacancies—while the τ_1 component turns out to be shorter than τ_{bulk} (annihilation in the bulk), due to the effect of trapping in defects, with respective intensities I_2 and I_1. Using the STM, we calculated the bulk lifetime in both samples of ~365 ps. This lifetime value may be too high to be ascribed to bulk annihilation. An alternative explanation is that the studied samples contain two distinct types of defects: FA vacancies or FA-I divacancies, which account for the large τ_2 value, and other defect types such as iodine or lead vacancies responsible for the shorter τ_1 component, which is close to the estimated bulk lifetime τ_{bulk}. This hypothesis will be further investigated through additional measurements and theoretical calculations. The rate of positron trapping to the defect κ_D (Table 1) and the vacancy density n are also determined by using the STM (Methods S2). Calculated vacancy number densities N are consistent for both samples, around $\sim1\times10^{15}$ cm^{-3}. This suggests that TEMPO predominantly passivates grain boundary and surface defects, which PALS may not detect in these samples, as mentioned earlier since the crystal grains are much larger than the positron diffusion length. FAPI-TEMPO samples exhibit high-quality crystals with defect concentrations one to two orders of magnitude lower than those reported for other halide perovskite materials, such as various MAPI samples, with defect densities between 6×10^{16} and 2×10^{17} cm^{-3}, that were attributed by Keeble et al. to Pb vacancies (V_{Pb}), calculated using the same defect-specific trapping coefficient (μ_V = 2×10^{15} s^{-1}).[69]

In addition, the XPS depth profiles in Figure S17 reveal that the addition of TEMPO to FAPI does not lead to significant changes in the overall elemental distribution of iodine, nitrogen, or lead across the perovskite layer and TiO_2 interface. This indicates that both FAPI and FAPI-TEMPO films maintain a consistent chemical structure through the depth of the films, suggesting that chemical states of the constituents remain similar, which align with the bulk defect analyses employing PALS. However, the slight variations observed, particularly for iodine and nitrogen, suggest that TEMPO might subtly influence interfacial properties, promoting uniformity while preserving the bulk composition. Furthermore, the presence of TEMPO during film formation may influence the adsorption and diffusion dynamics of precursor species. In agreement with the Shannon entropy

Table 1. Experimental positron lifetime results for the studied FAPI and FAPI-TEMPO samples

Sample	τ_1 [ps]	I_1 [%]	τ_2 [ps]	I_2 [%]	τ_{ave} [ps]	τ_{bulk} [ps]	κ_D [10^8 s^{-1}]	n [10^{-8}]	N [10^{15} cm^{-3}]
FAPI	353(4)	84(3)	452(9)	16(3)	368(5)	365(5)	1.0(8)	5.0(9)	1.0(3)
FAPI- TEMPO	346(4)	75(3)	436(9)	25(3)	368(5)	364(5)	1.5(9)	7.3(9)	1.5(3)

Positron lifetime values (τ_1 and τ_2) and intensity values (I_1 and I_2) values of the two components, average (τ_{ave}) and bulk lifetimes (τ_{bulk}), positron trapping rate (κ_D), defect concentration (n), and defect number density (N) are presented. The values were calculated as an average between the values at two positron implantation energies, 6.5 and 8 keV (around the maximum implantation fraction into the studied films, see Figure S15).

analyses in Figure 1, the diffusion of ionic species at the liquid/solid interface is modulated in the presence of TEMPO, leading to a more uniform and isotropic growth envelope. This controlled crystallization dynamic reduces anisotropic growth tendencies and spatial inhomogeneities, contributing to a more structurally and compositionally uniform film. These effects collectively reduce compositional fluctuations, enhance interfacial stability, and ultimately improve optoelectronic properties and long-term device performance as demonstrated above.

Concluding remarks

This study demonstrates the successful integration of TEMPO-based bulk passivation with FIRA to significantly enhance the stability and performance of FAPI PSCs. By introducing TEMPO into the FAPI precursor solution, we notably improved film crystallization leading to an enhanced film quality and photovoltaic efficiency, reaching a PCE of over 20%. Through detailed analysis, including steady-state and time-resolved PL, profilometry, and PALS, we provided insights into the role of TEMPO in reducing recombination centers and improving charge-carrier dynamics.

The results confirm that TEMPO primarily influences grain boundaries and surface defects, enhancing device stability under long-term operational and environmental stress. The devices demonstrated remarkable stability according to the used adapted ISOS protocols, with a low average degradation rate for TEMPO-treated samples and consistently better performance after 4,296 h under operational conditions than the studied control devices.

Notably, the aforementioned advantages were achieved without altering the bulk crystalline microstructure and its defect environment of the studied FAPI and FAPI-TEMPO films grown by FIRA possess. This work demonstrates depth-profiling positron lifetime spectroscopy as a powerful method for quantifying vacancy concentrations in metal halide perovskites films, enabling the detection and identification of neutral or negatively charged vacancy-related defects. These findings align and complement atomic-resolution transmission electron microscopy results, which highlight vacancies as influential defects in the studied system,[70] while PALS also provides a valuable quantitative perspective.

Quantitative analysis via PALS reveals that vacancy defects, characterized by a positron lifetime of 444(9) ps, serve as the primary positron traps attributed to FA vacancies or FA-I divacancies in both FAPI and FAPI+TEMPO perovskite films. The comparison between samples with and without the TEMPO additive (Table 1) confirms that vacancy concentrations remain unchanged at a relatively low level—about one vacancy per 10 million lattice sites. A higher concentration of lead vacancies is also a plausible scenario and will be the subject of further investigation. This is significantly lower than in MAPI samples, where vacancy density is one to two orders of magnitude higher due to the proposed cation lead vacancies (V_{Pb}).[69] These results highlight the effectiveness of the rapid annealing approach in achieving low defect densities and confirm that the TEMPO additive does not compromise this benefit.

These promising results open pathways for future studies exploring the impact of molecular additives on perovskite stability at different processing scales. This work establishes TEMPO as a valuable additive for advancing FAPI perovskite technology and supports the use of rapid photonic processing methods in the sustainable commercialization of high-efficiency, durable perovskite solar cells.

METHODS

Perovskite device preparation

Photovoltaic devices were fabricated on FTO-coated glass (Pilkington NSG TEC). The substrates were cleaned using a Hellmanex solution (2% in water), followed by 30 min sonication in a similar Hellmanex 2% water solution, 15 min sonication in IPA, and 5 min of oxygen plasma etching. Then, a 30 nm-thick compact TiO_2 layer was deposited onto FTO by spray pyrolysis at 450°C from a 0.1 M precursor solution of titanium diisopropoxide bis (acetylacetonate) in anhydrous ethanol and acetylacetone. After spraying, the FTO substrates were left at 450°C for 5 min before cooling to room temperature. A mesoporous TiO_2 layer was deposited by spin coating for 10 s at 4,000 rpm with a ramp of 2,000 rpm, using a 30 nm particle-size TiO_2 paste (Dyesol 30 NR-D) diluted in ethanol to 75 mg mL^{-1}, to produce a 150 to 200 nm-thick mesoporous layer. After spin coating, the FTO substrates were dried at 100°C for 10 min, and the films were annealed using a programmable hotplate (2,000 W, Harry Gestigkeit GmbH) to crystallize TiO_2 at 450°C for 30 min under a flow of dry air. All the organic salts were acquired from Greatcell Solar, while TCI provided lead halides and Merck provided DMSO and DMF solvents. The hybrid perovskite precursor solutions were deposited from a precursor solution containing FAI and PbI_2 (1.5 M) in anhydrous DMF/DMSO 3:1 (v/v). 1 mol % TEMPO was added to the solution precursors for the FAPI-TEMPO condition.

The films made using the FIRA method include spin coating of the perovskite solution in a single step at 4,000 rpm for 10 s. The substrates were then IR irradiated with a 640 ms pulse in the FIRA oven, pulling them out immediately after the heating. The films were then placed on a hotplate at 100°C for 15 min to complete solvent removal. FIRA processing was carried out in a glovebox filled with a N_2 atmosphere. Details of the FIRA setup have been reported elsewhere.[19]

A solution containing 2 mg mL^{-1} phenethylammonium iodide in isopropanol was dropped onto the perovskite film once the spin

coating started at acceleration of 1,200 m/s^2, speed of 4,000 rpm, and over the duration of 10 s. Then the films were placed onto a hotplate at 100°C for 25 min for complete solvent removal, mostly for the part from edged FTO where the IR irradiation doesn't heat up the sample. Immediately after cooling the perovskite films, a spiro-OMeTAD (Merck) solution (70 × 10^{-3} M in chlorobenzene) was deposited by spin coating at 4,000 rpm for 20 s. Spiro-OMeTAD was doped with Li-TFSI (Sigma Aldrich) and 4-*tert*-butylpyridine (TBP, Sigma-Aldrich). The molar ratios of the additives to spiro-OMeTAD were 0.5 and 3.3 for Li-TFSI and TBP, respectively. Finally, an 80 nm-thick gold layer was evaporated on the top of the film using a Leika system, in a vacuum of 10^{-4} Pa

Device characterization

For photovoltaic measurements, a solar simulator from ABET Technologies (Model 11016 Sun 2000) using a xenon arc lamp was used, and the solar cell response was recorded using a Metrohm PGSTAT302N Autolab. The intensity of the solar simulator was calibrated to 100 mW cm^{-2} using a silicon reference cell from ReRa Solutions (KG5 filtered). The reference cell was calibrated, and the *J–V* curves were measured using reverse and forward biases at a scan rate of 10 mV s^{-1} and a dwell time of 2 s; this slow scan rate was used in all *JV* measurements to minimize hysteresis effects. A black, non-reflective metal mask with an aperture area of 0.1024 cm^2 was used to cover the active area of the device. In this way, the active area of the devices was fixed, avoiding artifacts produced by scattered light. IPCE spectra was measured using a commercial apparatus (Arkeo-Ariadne, Cicci Research s.r.l.) based on a 300 W Xenon lamp and able to acquire the spectrum from 300 to 1,100 nm with 2 nm of resolution. It was recorded as a function of the wavelength at a constant white light bias of approximately 5 mW cm^{-2} supplied by an array of white-light emitting diodes. All measurements were conducted using a non-reflective metal mask with an aperture area of 0.3364 cm^2 to cover the active area of the device (0.3360 cm^2) and avoid light scattering through the sides. The size of the mask aperture and the active contact area of the devices were measured using an optical microscope with a 5× objective lens. Solar cell current transient dynamics (potentiostatic) and the maximum power point tracking data were measured under 1 sun equivalent white LED illumination using an SP300 Biologic potentiostat. The maximum power point tracking was performed using a home-developed program, keeping the devices at a maximum power point by creeping oscillation in voltage and measuring a full *JV* curve every 10 min. The devices were placed inside an in-house-developed airtight sample holder, which allowed them to be kept under an inert, nitrogen atmosphere. Additionally, the backside metal electrode of the devices was placed against a Peltier element, which, with the use of a PID (proportional-integral-derivative) controller, would keep the actual temperature of the device at 35°C regardless of the illumination or ambient temperature.

Materials characterization

SEM was carried out using a Tescan MIRA 3 LMH with a field emission source operated at an acceleration voltage of 10 kV. Film X-ray diffraction was performed in reflection spin mode using an Empyrean system (Theta–Theta, 240 mm) equipped with a PIXcel-1D detector, and Bragg–Brentano beam optics (including a hybrid monochromator). GIWAXS images were collected at an incident angle of 2° using a Bruker Discover Plus equipped with a rotating anode and a Dectris Eiger2 500 K detector operating in the 2D mode. Collimating optics of 300 microns were used to select the beam shape. Optical transmission measurements were performed using a Zeiss Axio-Scope A1 Pol with Zeiss EC Epiplan-Apochromat 10×, 50×, and 100× objectives and a Xenon light source (Ocean Optics HPX-2000). For spectroscopic measurements, an optical fiber (QP230-2-XSR, 230 μm core) collected the transmitted light from the sample. The spectra were recorded using a spectrometer (Ocean Optics Maya2000 Pro). All spectra were obtained at room temperature in transmission. The TRPL spectra were recorded using a LifeSpec II TCSPC (Edinburgh Instruments) with 506 nm excitation wavelength and stopping at 104 counts. The photon flux per pulse was 1.17 × 10^{10} photons per cm^2. The temperature of the perovskite film in the annealing chamber was measured using a CT-SF22-C3 Miniature Infrared Pyrometer and a germanium window for IR transmission. The temperature range is −50°C to 975°C with an optical resolution of 22:1, a spectral range of 8–14 μm, a focus of 0.6 mm at 10 mm distance, a response time of 150 ms, a temperature resolution of 0.1°C, a system accuracy of ±1% or ±1°C, an emissivity/gain of 0.100–1.100, and a transmissivity/gain of 0.100–1.100. The distance from the front edge of the CT-SF22 device to the measurement object is 30 mm, and this distance from the spot size has a diameter of 5 mm. A PID regulation mode was set to control the power of the lamps, where the output signal taken using a pyrometer will oscillate around the set point with a decaying sinusoidal amplitude. A LabVIEW GUI adjusts the PID values for the larger sinusoidal amplitude ending in shorter ones to guarantee a stable system.

For the profilometry analysis, we used a DektakXT stylus surface profiler. Being available with an automatic *X–Y* and theta stage, it provides a step-height repeatability of 5 Å. The stylus is linked to a linear variable differential transformer, and the Vision64 application calculates and displays the results of user-selected analytical functions for measuring the surface texture and other parameters to characterize the profile data. The measurement was set up with a high-resolution range of 6 μm in the *z* axis, 0.07 μm s^{-1} scan rate, 1,000 traces, and a stylus radius of 7 μm

The positron lifetime experiments were performed at the mono-energetic positron spectroscopy beamline of the radiation source ELBE (electron linac for beams with high brilliance and low emittance) at Helmholtz-Zentrum Dresden-Rossendorf (Germany).[71] In this study, PALS is used with a bunched slow-positron beam. Positrons were monoenergetically implanted at various depths in the sample using a variable energy positron beam ranging between 1 and 16 keV. The measurements were carried out at room temperature in vacuum condition (10^{-7} mbar). A digital lifetime $CeBr_3$ scintillator detector operated by a homemade software, utilizing a SPDevices ADQ14DC-2X digitizer with 14-bit vertical resolution and 2 GS s^{-1} horizontal resolution, was used (the overall time resolution was about 230 ps). The resolution function required for spectrum analysis was composed of two Gaussian functions with distinct intensities depending on the positron implantation energy and appropriate

relative shifts. All spectra contain at least 1×10^7 counts and a time calibration of 3 ps per channel. The lifetime spectra were analyzed as a sum of time-dependent exponential decays according to Equation 2, convoluted with the spectrometer timing resolution using a nonlinear least square approach provided by the PALSfit software.[67]

High-throughput data acquisition

The data acquisition system provided micron-scale precision for optical observation and analysis. Measurements were performed using a microscope (Olympus, BX3M) equipped with a 5× objective (Olympus, MPLN5X-1-7). For illumination, a white LED (OMICRON, LEDMOD) was coupled to the microscope's illuminator, and images were captured with a high-resolution 2,048 × 2,048 pixel CMOS camera (Hamamatsu, ORCA-FLASH 4.0 LT). To enhance throughput, the system incorporated a custom-developed microdevice manager for stage control, implemented via a Python script. The setup featured a high-speed XYZ scanning stage (MLS203-1, Thorlabs), capable of scanning an entire holder containing up to eight films within 45 min. Each film measured 25 × 17 mm, with an active area of approximately 15 × 13 mm subjected to detailed scanning. With a 5× objective, the field of view typically spans 2.4 × 2.4 mm. A step size of 2.3 mm in both X and Y directions was selected to ensure efficient imaging of the entire area while minimizing redundancy. Focus adjustments for the z axis were performed manually at a single scanning spot on the sample and then automatically applied across the remaining scan areas. This protocol ensured comprehensive coverage of the sample area, maintaining high spatial resolution and efficiency.

Image processing

Shannon entropy and CID are applied to quantify structural homogeneity. See Methods S1 for further details. Shannon entropy measures the disorder within an image, as a metric of structural uniformity. At the same time, CID calculates the regularity by analyzing the ratio of compressed to original image length, indicating image consistency.

Entropy maps were generated by computing the Shannon entropy of grayscale intensity distributions using a histogram-based approach. For each image, pixel intensity values were converted to a probability distribution, and entropy was calculated as:

\begin{equation}

$$H(X) = -\sum_{\{x_i\}} p(x_i) \log_2 p(x_i)$$

\end{equation}

where $-\{x_i\}$ represents the set of possible pixel intensity values, and $p(x_i)$ is their probability distribution. Local entropy deviation maps were generated by computing the entropy within a sliding window across the image, capturing spatial variations in homogeneity.

To enhance the visualization of these variations, both heat maps and local entropy deviation maps were computed. The heat maps provide a colormap-enhanced representation of entropy values, improving contrast between regions of differing structural uniformity.

Additionally, coefficient of variation (CV) is used on segmented sample images to assess crystal area and perimeter variability, with CV values reflecting relative homogeneity across the samples. Circularity distortion (CD) analysis is conducted to further characterize crystal shape consistency, measuring deviations from ideal circular structures. It is a parameter of the uniformity of radial growth in the crystals. These metrics assess film homogeneity, allowing for precise differentiation between the structural qualities of FAPI and FAPI-TEMPO samples.

RESOURCE AVAILABILITY

Lead contact

Further information and requests for resources and reagents should be directed to and will be fulfilled by the lead contact, Sandy Sánchez-Alonso (sandy.sanchezalonso@epfl.ch).

Materials availability

This study did not generate new unique chemical reagents. All precursor salts (FAI and PbI_2), solvents (DMF and DMSO), and the TEMPO additive are commercially available, as detailed in the methods section. Custom thin-film samples (FAPI and FAPI-TEMPO) and complete N-i-P solar-cell devices produced in this work can be provided by the lead contact upon reasonable request and completion of a material-transfer agreement (MTA).

Data and code availability

- All data supporting the findings of this study are included in the main text or the supplemental information.
- The complete raw datasets including stability-test logs, TRPL/PLQY transients, surface-profilometry, positron-annihilation lifetime spectra, XPS depth profiles, and the pixel-defect detection algorithms are openly available in this repository: https://doi.org/10.5281/zenodo.15324373
- Any additional information required to reanalyze the data reported in this paper is available from the lead contact upon request.

ACKNOWLEDGMENTS

S.S.-A. gratefully acknowledges the funding and support of the Swiss SNF Bridge-Discovery Project (grant no. 40B2-0_203626), Automated Photonic-pulses Processing for Thin Solar Energy Devices (A3P), and the EU HORIZON-CL5-2022-D3-03-05project no. 101122345, and High-Efficiency Perovskites on Flexible Substrates for Sustainable Applications (HEPAFLEX). Parts of this research were carried out at ELBE at the Helmholtz-Zentrum Dresden – Rossendorf e.V., a member of the Helmholtz Association. We would like to thank the facility staff for assistance, especially Maciej Oskar Liedke, Andreas Wagner, Maik Butterling, and Eric Hirschmann for their valuable contributions to the PALS measurements and subsequent analyses.

AUTHOR CONTRIBUTIONS

Conceptualization, S.S.-A.; methodology, S.S.-A. and L.P.; investigation, S.S.-A., L.P., F.T.E. (PLQY), R.F. (PALS), O.V., C.G., and J.H. (pixel-detection algorithms); writing – original draft, S.S.-A.; writing – review & editing, S.S. and L.P.; resources, K.S. and M.G.; supervision, S.S.-A., K.S., and M.G.

DECLARATION OF INTERESTS

The authors declare no competing interests.

SUPPLEMENTAL INFORMATION

Supplemental information can be found online at https://doi.org/10.1016/j.joule.2025.101972.

Received: December 19, 2024
Revised: March 3, 2025
Accepted: May 9, 2025
Published: May 21, 2025

REFERENCES

1. Shen, Y., Zhang, T., Xu, G., Steele, J.A., Chen, X., Chen, W., Zheng, G., Li, J., Guo, B., Yang, H., et al. (2024). Strain regulation retards natural operation decay of perovskite solar cells. Nature *635*, 882–889.
2. Qu, Z., Zhao, Y., Ma, F., Mei, L., Chen, X.-K., Zhou, H., Chu, X., Yang, Y., Jiang, Q., Zhang, X., and You, J. (2024). Enhanced charge-carrier transport and defects mitigation of passivation layer for efficient perovskite solar cells. Nat. Commun. *15*, 8620.
3. Zhu, X., Li, M., Mo, K., Yang, M., Li, S., Yang, Y., Wang, H., Li, R., Liu, Y., Lin, Q., and Wang, Z. (2024). A surface-reconstructed bilayer heterojunction enables efficient and stable inverted perovskite solar cells. Adv. Mater. *36*, 2409340.
4. Qu, S., Huang, H., Wang, J., Cui, P., Li, Y., Wang, M., Li, L., Yang, F., Sun, C., Zhang, Q., et al. (2025). Revealing and inhibiting the facet-related ion migration for efficient and stable perovskite solar cells. Angew. Chem. Int. Ed. *64*, e202415949.
5. Yang, C., Hu, W., Liu, J., Han, C., Gao, Q., Mei, A., Zhou, Y., Guo, F., and Han, H. (2024). Achievements, challenges, and future prospects for industrialization of perovskite solar cells. Light Sci. Appl. *13*, 227.
6. Chen, P., Xiao, Y., Li, S., Jia, X., Luo, D., Zhang, W., Snaith, H.J., Gong, Q., and Zhu, R. (2024). The promise and challenges of inverted perovskite solar cells. Chem. Rev. *124*, 10623–10700.
7. Ahmad, S., Kazim, S., and Grätzel, M. (2022). Perovskite Solar Cells: Materials, Processes, and Devices (Wiley).
8. Fujiwara, H. (2022). Hybrid Perovskite Solar Cells: Characteristics and Operation (Wiley).
9. Suo, J., Yang, B., Mosconi, E., Bogachuk, D., Doherty, T.A.S., Frohna, K., Kubicki, D.J., Fu, F., Kim, Y., Er-Raji, O., et al. (2024). Multifunctional sulfonium-based treatment for perovskite solar cells with less than 1 % efficiency loss over 4,500-h operational stability tests. Nat. Energy *9*, 172–183.
10. Jeong, J., Kim, M., Seo, J., Lu, H., Ahlawat, P., Mishra, A., Yang, Y., Hope, M.A., Eickemeyer, F.T., Kim, M., et al. (2021). Pseudo-halide anion engineering for α-$FAPbI_3$ perovskite solar cells. Nature *592*, 381–385.
11. Zheng, Z., Wang, S., Hu, Y., Rong, Y., Mei, A., and Han, H. (2022). Development of formamidinium lead iodide–based perovskite solar cells: efficiency and stability. Chem. Sci. *13*, 2167–2183.
12. Yin, Y., Zhou, Y., Fu, S., Lin, Y.–C., Zuo, X., Raut, A., Zhang, Y., Tsai, E.H. R., Li, M., Lu, F., et al. (2024). Template-assisted growth of high-quality α-phase $FAPbI_3$ crystals in perovskite solar cells using thiol-functionalized MoS_2 nanosheets. ACS Nano *18*, 30816–30828.
13. Vanni, N., Pò, R., Biagini, P., Bravetti, G., Carallo, S., Giuri, A., and Rizzo, A. (2024). Formamidinium perovskite deposition in ambient-air environment for inverted p-i-n solar cells. Nanomaterials *14*, 107.
14. Leblanc, A., Mercier, N., Allain, M., Dittmer, J., Pauporté, T., Fernandez, V., Boucher, F., Kepenekian, M., and Katan, C. (2019). Enhanced stability and band-gap tuning of α-$[HC(NH_2)_2]PbI_3$ hybrid perovskite by large-cation integration. ACS Appl. Mater. Interfaces *11*, 20743–20751.
15. Gawlińska-Nęcek, K., Kot, M., Starowicz, Z., Jarzębska, A., Panek, P., and Flege, J.I. (2024). Instability of formamidinium lead iodide (FAPI) deposited on a copper oxide hole-transporting layer. ACS Appl. Mater. Interfaces *16*, 27936–27943.
16. Shen, W., Cai, H., Kong, Y., Dong, W., Bai, C., Liang, G., Li, W., Zhao, J., Huang, F., Cheng, Y.B., and Zhong, J. (2023). Protic amine carboxylic-acid ionic-liquid additives regulate α-$FAPbI_3$ phase transition for high-efficiency perovskite solar cells. Small *19*, e2302194.
17. Liang, Y., Li, F., Cui, X., Lv, T., Stampfl, C., Ringer, S.P., Yang, X., Huang, J., and Zheng, R. (2024). Toward stabilization of formamidinium lead iodide perovskites by defect control and composition engineering. Nat. Commun. *15*, 1707.
18. Cui, X., Jin, J., Tai, Q., and Yan, F. (2022). Recent progress on the phase stabilization of $FAPbI_3$ for high-performance perovskite solar cells. Sol. RRL *6*, 2200497.
19. Sánchez, S., Cacovich, S., Vidon, G., Guillemoles, J.-F., Eickemeyer, F., Zakeeruddin, S.M., Schawe, J.E.K., Löffler, J.F., Cayron, C., Schouwink, P., and Graetzel, M. (2022). Thermally controlled growth of photoactive $FAPbI_3$ films for highly stable perovskite solar cells. Energy Environ. Sci. *15*, 3862–3876.
20. Sánchez, S., Hua, X., Günzler, A., Bermúdez-Ureña, E., Septiadi, D., Saliba, M., and Steiner, U. (2020). Flash infrared pulse time control of perovskite crystal nucleation and growth from solution. Cryst. Growth Des. *20*, 670–679.
21. Lufaso, M.W., and Woodward, P.M. (2004). Jahn–Teller distortions, cation ordering and octahedral tilting in perovskites. Acta Crystallogr. B *60*, 10–20.
22. Sánchez, S., Carlsen, B., Škorjanc, V., Flores, D.N., Serafini, P., Mora-Seró, I., Schouwink, P., Zakeeruddin, S.M., Grätzel, M., and Hagfeldt, A. (2021). Thermodynamic stability screening of IR-photonic processed multication halide perovskite thin films. J. Mater. Chem. A Mater. *9*, 26885–26895.
23. Hautzinger, M.P., Mihalyi-Koch, W., and Jin, S. (2024). A-site cation chemistry in halide perovskites. Chem. Mater. *36*, 10408–10420.
24. Book chapter Sánchez-Alonso, S., and Pfeifer, L. (2023). Structure, composition and stability of metal-halide perovskites. In Metal Halide Perovskites for Generation, Manipulation and Detection of Light, J.P. Martínez-Pastor, P.P. Boix, and G. Xing, eds. (Elsevier), pp. 3–47.
25. Kahmann, S., Nazarenko, O., Shao, S., Hordiichuk, O., Kepenekian, M., Even, J., Kovalenko, M.V., Blake, G.R., and Loi, M.A. (2020). Negative thermal quenching in $FASnI_3$ perovskite single crystals and thin films. ACS Energy Lett. *5*, 2512–2519.
26. Vigliotti, A., and Pasini, D. (2012). Stiffness and strength of tridimensional periodic lattices. Comput. Methods Appl. Mech. Eng. *229–232*, 27–43.
27. Sánchez-Alonso, S., Steiner, U., and Hua, X. (2019). Phase evolution during perovskite formation—insight from pair-distribution-function analysis. Chem. Mater. *31*, 3498–3506.
28. McCall, K.M., Stoumpos, C.C., Kostina, S.S., Kanatzidis, M.G., and Wessels, B.W. (2017). Strong electron–phonon coupling and self-trapped excitons in the defect halide perovskites $A_3M_2I_9$ (A = Cs, Rb; M = Bi, Sb). Chem. Mater. *29*, 4129–4145.
29. Zhou, L., Katan, C., Nie, W., Tsai, H., Pedesseau, L., Crochet, J.J., Even, J., Mohite, A.D., Tretiak, S., and Neukirch, A.J. (2019). Cation alloying delocalizes polarons in lead-halide perovskites. J. Phys. Chem. Lett. *10*, 3516–3524.
30. Neukirch, A.J., Abate, I.I., Zhou, L., Nie, W., Tsai, H., Pedesseau, L., Even, J., Crochet, J.J., Mohite, A.D., Katan, C., and Tretiak, S. (2018). Geometry distortion and small polaron binding-energy changes with ionic substitution in halide perovskites. J. Phys. Chem. Lett. *9*, 7130–7136.
31. Pool, V.L., Dou, B., Van Campen, D.G., Klein-Stockert, T.R., Barnes, F.S., Shaheen, S.E., Ahmad, M.I., van Hest, M.F.A.M., and Toney, M.F. (2017). Thermal engineering of $FAPbI_3$ perovskite material via radiative thermal annealing and in situ XRD. Nat. Commun. *8*, 14075.
32. Penpong, K., Seriwatanachai, C., Naikaew, A., Phuphathanaphong, N., Thant, K.K.S., Srathongsian, L., Sukwiboon, T., Inna, A., Sahasithiwat, S., Pakawatpanurut, P., et al. (2023). Robust perovskite formation via vacuum thermal annealing for indoor perovskite solar cells. Sci. Rep. *13*, 10933.
33. Sánchez, S., Pfeifer, L., Vlachopoulos, N., and Hagfeldt, A. (2021). Rapid hybrid perovskite film crystallization from solution. Chem. Soc. Rev. *50*, 7108–7131.

34. Sánchez, S., Jerónimo-Rendón, J., Saliba, M., and Hagfeldt, A. (2020). Highly efficient and rapid manufactured perovskite solar cells via Flash InfraRed Annealing. Mater. Today *35*, 9–15.

35. Ling, P.S.V., Hagfeldt, A., and Sánchez, S. (2021). Flash Infrared Annealing for Perovskite Solar Cell Processing. J. Vis. Exp. *171*, e61730.

36. Sánchez, S., Vallés-Pelarda, M., Alberola-Borràs, J.A., Vidal, R., Jerónimo-Rendón, J.J., Saliba, M., Boix, P.P., and Mora-Seró, I. (2019). Flash infrared annealing as a cost-effective and low-environmental-impact processing method for planar perovskite solar cells. Mater. Today *31*, 39–46.

37. Sánchez, S., Hua, X., Phung, N., Steiner, U., Abate, A., and Saliba, M. (2018). Flash Infrared Annealing for Antisolvent-Free Highly Efficient Perovskite Solar Cells. Adv. Energy Mater. *8*, 1702915.

38. Sánchez, S., Neururer, C., Grobéty, B., Phung, N., Steiner, U., Saliba, M., and Abate, A. (2018). Efficient and stable inorganic perovskite solar cells manufactured by pulsed flash infrared annealing. Adv. Energy Mater. *8*, 1802060.

39. Serafini, P., Boix, P.P., Barea, E.M., Edvinson, T., Sánchez, S., and Mora-Seró, I. (2023). Photonic processing of $MAPbI_3$ films by flash annealing and rapid growth for high-performance perovskite solar cells. Sol. RRL *7*, 2200893.

40. Muscarella, L.A., Hutter, E.M., Sánchez, S., Dieleman, C.D., Savenije, T.J., Hagfeldt, A., Saliba, M., and Ehrler, B. (2019). Crystal orientation and grain size: do they determine optoelectronic properties of $MAPbI_3$ perovskite? J. Phys. Chem. Lett. *10*, 6010–6018.

41. Szostak, R., Sánchez, S., Marchezi, P.E., Marques, A.S., Silva, J.C., Holanda, M.S., Hagfeldt, A., Tolentino, H.C.N., and Nogueira, A.F. (2021). Revealing the perovskite film formation using the gas quenching method by in situ GIWAXS: morphology, properties, and device performance. Adv. Funct. Mater. *31*, 2007473.

42. Tuomisto, F., and Makkonen, I. (2013). Defect identification in semiconductors with positron annihilation: experiment and theory. Rev. Mod. Phys. *85*, 1583–1631.

43. Riontino, G., Lussana, D., Massazza, M., Barucca, G., Mengucci, P., and Ferragut, R. (2008). Structure evolution of EV31 Mg alloy. J. Alloys Compd. *463*, 200–206.

44. Barucca, G., Ferragut, R., Lussana, D., Mengucci, P., Moia, F., and Riontino, G. (2009). Phase transformations in QE22 Mg alloy. Acta Mater. *57*, 4416–4425.

45. Riontino, G., Massazza, M., Ferragut, R., Lussana, D., and Somoza, A. (2002). Secondary ageing in Al–Cu–Mg. Philos. Mag. Lett. *82*, 495–502.

46. Sajjadi, M., Jamali, R., Kiyani, T., Mohamadnia, Z., and Moradi, A.-R. (2024). Characterization of Schiff base self-healing hydrogels by dynamic speckle pattern analysis. Sci. Rep. *14*, 27950.

47. Zarghami, S.A. (2023). Deviation from a state of perfect uniformity: an indicator of structural complexity in projects. Syst. Res. Behav. Sci. *40*, 488–500.

48. Pietrosanto, M., Adinolfi, M., Guarracino, A., Ferrè, F., Ausiello, G., Vitale, I., and Helmer-Citterich, M. (2021). Relative Information Gain: Shannon entropy-based measure of the relative structural conservation in RNA alignments. NAR Genom. Bioinform. *3*, lqab007.

49. Shannon, C.E. (1948). A mathematical theory of communication. Bell Syst. Tech. J. *27*, 379–423.

50. He, J., Fang, W.-H., Long, R., and Prezhdo, O.V. (2018). Increased lattice stiffness suppresses nonradiative charge recombination in $MAPbI_3$ doped with larger cations: time-domain ab initio analysis. ACS Energy Lett. *3*, 2070–2076.

51. Brakkee, R., and Williams, R.M. (2020). Minimizing defect states in lead-halide perovskite solar-cell materials. Appl. Sci. *10*, 3061.

52. Barker, A.J., Sadhanala, A., Deschler, F., Gandini, M., Senanayak, S.P., Pearce, P.M., Mosconi, E., Pearson, A.J., Wu, Y., Srimath Kandada, A. R., et al. (2017). Defect-assisted photo-induced halide segregation in mixed-halide perovskite thin films. Preprint at arXiv. https://doi.org/10.48550/arXiv.1703.04232.

53. Zhang, H., Pfeifer, L., Zakeeruddin, S.M., Chu, J., and Grätzel, M. (2023). Tailoring passivators for highly efficient and stable perovskite solar cells. Nat. Rev. Chem *7*, 632–652.

54. Chen, X., Cai, W., Niu, T., Wang, H., Liu, C., Zhang, Z., Du, Y., Wang, S., Cao, Y., Liu, P., et al. (2024). Crystallization control via ligand–perovskite coordination for high-performance flexible perovskite solar cells. Energy Environ. Sci. *17*, 6256–6267.

55. Wang, Z., Yang, C., Cui, Y., Xie, L., and Hao, F. (2022). Acetone complexes for high-performance perovskite photovoltaics with reduced non-radiative recombination. Mater. Adv. *3*, 2047–2055.

56. Alberti, A., Smecca, E., Valastro, S., Deretzis, I., Mannino, G., Bongiorno, C., Fisicaro, G., and La Magna, A. (2022). Perovskite solar cells from the viewpoint of innovation and sustainability. Phys. Chem. Chem. Phys. *24*, 21549–21566.

57. Miao, S., Yuan, S., Zhu, D., Cai, Q., Wang, H.Y., Wang, Y., Qin, Y., and Ai, X.C. (2022). Mesoporous TiO_2 layer suppresses ion accumulation in perovskite solar cells. Phys. Chem. Chem. Phys. *24*, 20689–20693.

58. Sánchez, S., and Hagfeldt, A. (2021). Flash infrared annealing for processing of perovskite solar cells. In Perovskite Solar Cells, M. Grätzel, S. Ahmad, and S. Kazim, eds. (Wiley), pp. 33–89.

59. Jiang, Q., Zhao, Y., Zhang, X., Yang, X., Chen, Y., Chu, Z., Ye, Q., Li, X., Yin, Z., and You, J. (2019). Surface passivation of perovskite film for efficient solar cells. Nat. Photonics *13*, 460–466.

60. Chao, I.-H., Yang, Y.-T., Yu, M.-H., Chen, C.-H., Liao, C.-H., Lin, B.-H., Ni, I.-C., Chen, W.-C., Ho-Baillie, A.W.Y., and Chueh, C.-C. (2023). Performance enhancement of lead-free 2D tin-halide perovskite transistors by surface passivation and its impact on non-volatile photomemory characteristics. Small *19*, 2207734.

61. Lee, D.-K., Lim, K.-S., Lee, J.-W., and Park, N.-G. (2021). Scalable perovskite coating via anti-solvent-free Lewis acid–base adduct engineering for efficient perovskite solar modules. J. Mater. Chem. A *9*, 3018–3028.

62. Wu, Z., Cai, H., Wu, T., Xu, J., Wang, Z., Du, H., Zhao, J., Huang, F., Cheng, Y.B., and Zhong, J. (2024). The tricyclic alkaloid catalyzed crystallization of α-$FAPbI_3$ for high-performance antisolvent-free perovskite solar cells. Energy Environ. Sci. *17*, 4670–4680.

63. Zhu, H., Cai, T., Que, M., Song, J.-P., Rubenstein, B.M., Wang, Z., and Chen, O. (2018). Pressure-induced phase transformation and band-gap engineering of formamidinium lead iodide perovskite nanocrystals. J. Phys. Chem. Lett. *9*, 4199–4205.

64. Khenkin, M.V., Katz, E.A., Abate, A., Bardizza, G., Berry, J.J., Brabec, C., Brunetti, F., Bulović, V., Burlingame, Q., Di Carlo, A., et al. (2020). Consensus statement for stability assessment and reporting for perovskite photovoltaics based on ISOS procedures. Nat. Energy *5*, 35–49.

65. Niño, J.D., and Johnson, O.K. (2023). Influence of grain-boundary energy anisotropy on the evolution of grain-boundary network structure during 3D anisotropic grain growth. Comput. Mater. Sci. *217*, 111879.

66. Krause-Rehberg, R., and Leipner, H.S. (1999). Positron Annihilation in Semiconductors: Defect Studies (Springer).

67. Olsen, J.V., Kirkegaard, P., Pedersen, N.J., and Eldrup, M. (2007). PALSfit: A new program for the evaluation of positron-lifetime spectra. Phys. Status Solidi *4*, 4004–4006.

68. Frank, W., and Seeger, A. (1974). Theoretical foundation and extension of the trapping model. Appl. Phys. *3*, 61–66.

69. Keeble, D.J., Wiktor, J., Pathak, S.K., Phillips, L.J., Dickmann, M., Durose, K., Snaith, H.J., and Egger, W. (2021). Identification of lead-vacancy defects in lead-halide perovskites. Nat. Commun. *12*, 5566.

70. Rothmann, M.U., Kim, J.S., Cortés, P., Lohmann, K.B., O'Leary, C.M., Sheader, A.A., Clark, L., Snaith, H.J., Johnston, M.B., Nellist, P.D., and Herz, L.M. (2020). Atomic-scale microstructure of metal halide perovskite. Science *370*, eabb5940.

71. Wagner, A., Butterling, M., Liedke, M.O., Potzger, K., and Krause-Rehberg, R. (2018). Positron annihilation lifetime and Doppler-broadening spectroscopy at the ELBE facility. AIP Conf. Proc. *1970*, 030003.